A 3D Porous Inverse Opal Ni Structure on a Cu Current Collector for Stable Lithium-Metal Batteries

Soo Min Jeong,[a, b] Mihye Wu,[a] Tae Yeong Kim,[a] Dong Hwan Kim,[c] Se-Hee Kim,[a] Hong Kyoon Choi,[c] Yun Chan Kang,[b] and Do Youb Kim*[a]

Lithium (Li) metal is considered the best anode material for next-generation high-energy density Li-metal batteries. However, Li dendrite formation and growth hinder the practical applications of Li metal anodes. Herein, we report a three-dimensional (3D) porous inverse opal nickel structure on a copper foil current collector (Ni IO@Cu) that has a controllable pore size and thickness and is fabricated via colloidal self-assembly and electrodeposition. The uniform interconnected pores with a large surface area of the Ni IO@Cu structure can effectively dissipate high areal current densities, resulting in the stable formation of a solid electrolyte interface and dense, dendrite-free, flat lithium deposits. In comparison to the use of bare Cu, the use of the Ni IO@Cu current collector resulted in greatly improved stability and lowered the voltage hysteresis in various Li plating/stripping tests. Moreover, Li-ion battery and Li-sulfur battery full cells prepared using the Ni IO@Cu also displayed excellent cycling performance. This work further demonstrates the significance of the 3D porous structure for preparing dendrite-free Li metal anodes.

1. Introduction

In recent years, lithium (Li)-ion batteries (LIBs) have drawn significant attention because of the increasing demand for portable electronics, drones, robots, and, in particular, electric vehicles (EVs).[1–3] To extend the usability of these devices and the driving range in the case of EVs, increasing the energy density of LIBs is crucial. One way to enhance the energy density of LIBs is to reduce the mass or volume of the cell by using thinner and/or lighter separators, current collectors, and packing materials. Alternatively, the use of active materials having high capacities or large voltage differences for pairing can also achieve high energy densities.[4,5] Accordingly, various cathode materials with high specific capacities such as high-Ni cathode materials have been recently developed.[6–8] However, graphite, which has a relatively low theoretical specific capacity (372 mAh g^{-1}), is still the most commonly used anode material in current LIBs, and this limits further increases in the energy density of LIBs.[9,10]

Among the various available candidates, Li metal is believed to be the best anode material for LIBs because of its high specific capacity (3860 mAh g^{-1}), low redox potential (-3.04 V vs. the standard hydrogen electrode), and low density

(0.59 g cm^{-3}).[11,12] However, the replacement of graphite with Li metal as an anode material has been limited by several serious problems. Li metal is a "hostless" anode and undergoes huge volume changes during cycling; these changes reduce the mechanical stability of the electrode. In addition, the uncontrollable growth of Li dendrites causes the repeated destruction and formation of the solid electrolyte interphase (SEI), which consumes the electrolyte and decreases the coulombic efficiency (CE). Ultimately, the depletion of the electrolyte results cell death.[10–12] A more serious issue is that the Li dendrites can penetrate the polymer separator, causing short circuits and even explosions.[12,13] In addition, during the Li stripping process, the roots of the Li dendrites dissolve easily, and the Li dendrites are broken and isolated from the anode, thus forming "dead Li", which results in capacity fading.[10,14] These critical problems have prevented the development and application of durable Li metal batteries (LMBs), which have higher energy densities than conventional LIBs containing graphite-based anodes.

Over the past decades, great efforts have been made to solve the problems facing Li metal anode. From an electrolyte engineering point of view, the use of concentrated electrolytes,[15,16] electrolyte additives,[17,18] nanostructured electrolytes,[19,20] or solid electrolytes[21–23] has been proposed. In addition, the formation of artificial SEI/protective layer on Li metal anode[24–27] and separator modification[28–30] have been also reported as interface control strategies. On the other hand, the design of three-dimensional (3D) porous structures as hosts for Li is particularly attractive because 3D structures can not only effectively regulate Li deposition but also accommodate the volume changes of the Li anode.[31–35] Crucially, the large surface area of 3D structures provides more electrochemical reaction sites, enables faster electron transfer, and lowers the areal current density.[35] This can reduce the overpotentials

[a] S. M. Jeong, M. Wu, T. Y. Kim, Dr. S.-H. Kim, Dr. D. Y. Kim
     Energy Materials Research Center, KRICT
     141 Gajeong-ro, Yuseong-gu, 34114 Daejeon, Republic of Korea
     E-mail: dykim@krict.re.kr
[b] S. M. Jeong, Prof. Y. C. Kang
     Department of Materials Science and Engineering, Korea University
     145 Anam-ro, Seongbuk-gu, 02841 Seoul, Republic of Korea
[c] D. H. Kim, Prof. H. K. Choi
     Division of Advanced Materials Engineering, Kongju National University
     31080 Cheonan, Republic of Korea
     Supporting information for this article is available on the WWW under
     https://doi.org/10.1002/batt.202100257

during Li plating/stripping process and is beneficial for stable Li deposition and the suppression of Li dendrite growth. In addition to the stable Li deposition, the empty pores provide space for Li growth, thus moderating the huge volume changes of the Li anode. Accordingly, many studies have focused on Li stabilization using 3D porous structures, including metal foams,[36–38] metal meshes,[39,40] porous Cu,[32–34,41,42] and porous C.[31,43–47] These reports demonstrated that the use of 3D porous structures can effectively prevent the growth of Li dendrites, as well as the volume changes of Li, resulting in improved electrochemical performance. However, fine-tuning the structural features such as pore size and thickness, which can determine electrochemical performance, is still challenging.

In this paper, we report a 3D porous Ni inverse opal (IO) structure on Cu foil (Ni IO@Cu) for application in dendrite-free Li metal anodes. The Ni IO@Cu was fabricated by using the self-assembly of colloidal polystyrene (PS) particles, followed by the electrodeposition of Ni. Crucially, the pore size and thickness of resulting structures can be easily controlled by varying the size of colloidal particles and electrodeposition parameters, respectively. The high surface area and well-ordered pores of the 3D porous Ni IO@Cu effectively reduced the areal current density and prevented charge concentration. In addition, the Ni IO@Cu accommodated Li deposits on the surfaces of the interconnected pores of the structure. As a result, the Li deposits grown on the Ni IO@Cu current collector displayed a dense, dendrite-free, and flat morphology, whereas the Li deposited on a bare Cu current collector was porous and rough. Furthermore, the use of Ni IO@Cu resulted in much improved electrochemical performance in Li plating/stripping tests, yielding lower overpotentials during both nucleation and cycling, as well as a longer cycle life, compared to the use of the bare Cu current collector. Finally, LIB and Li-sulfur (S) battery cells were assembled using lithiated Ni IO@Cu as an anode and were found to exhibit far enhanced cycling stabilities in comparison to cells using lithiated bare Cu.

2. Results and Discussions

Figure 1(a) shows a schematic of the fabrication of the 3D porous Ni IO@Cu. Briefly, a 3D opal structure of colloidal PS particles on Cu foil was prepared by self-assembly. Ni was then used to fill the empty spaces between the PS particles using electrodeposition. Finally, the 3D porous Ni IO@Cu was obtained by washing off the PS colloidal crystal template with tetrahydrofuran. In this procedure, the colloidal PS particles having diameters of approximately 1 μm formed an ordered self-assembled structure on the Cu foil (Figure 1b), and the electrodeposition of Ni replicated the structure of the PS spheres, yielding a regular IO structure having interconnected pores of approximately 1 μm (Figure 1c). The insets in Figure 1(b and c) show photographs of the PS opal and Ni IO structures on the Cu foil, respectively, showing the structural colors, which indicate the large-area uniformity of the prepared structures. The thickness of the Ni IO structure obtained by electrodeposition at a current density of 0.4 mA cm^{-2} for 15,000 s was approximately 2.5 μm (Figure 1d). The XRD pattern acquired from the sample contained sharp peaks corresponding to crystalline Ni and Cu (JCPDS #03-1051 and #04-836, respectively), confirming the formation of Ni IO@Cu (Figure S1 in Supporting Information). Importantly, the pore size and thickness of the Ni IO structure can be easily and precisely controlled, unlike in previous studies,[31–34,36,37,39–41,43–45] by varying the size of colloidal PS crystal template and the Ni electrodeposition parameters, respectively (Figure S2).

To evaluate the ability of the material to stabilize Li deposition, the changes to the morphology of Li deposited on a bare Cu foil current collector and the Ni IO@Cu current
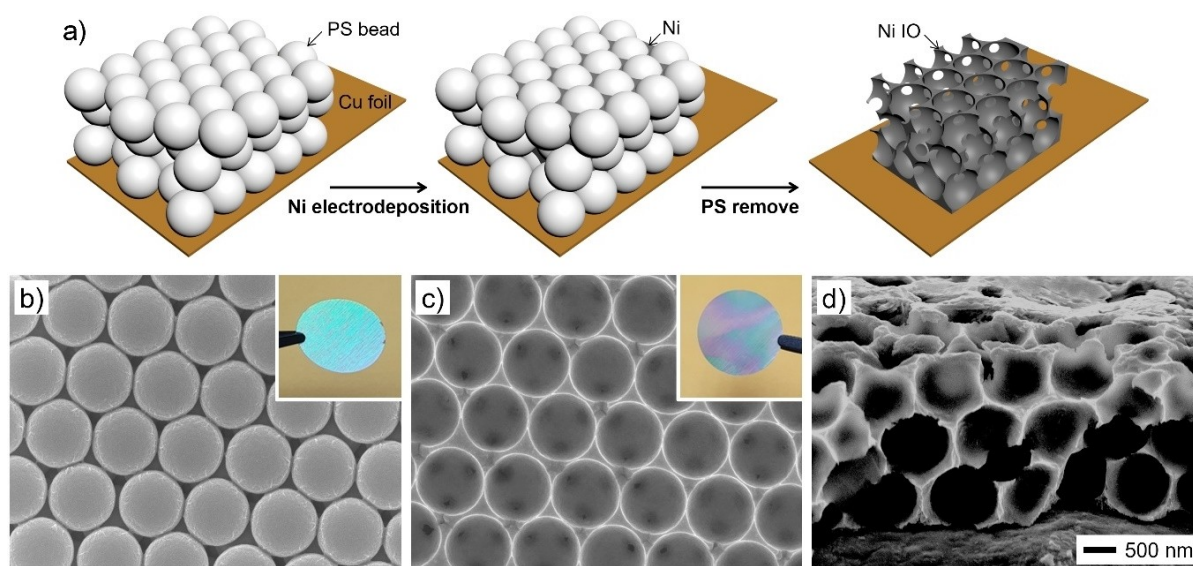

Figure 1. a) Schematic illustration for the fabrication of Ni IO@Cu. b) SEM images of PS opal structure, c) top and d) cross-sectional view SEM images of Ni IO@Cu. Insets in b) and c) show the corresponding photographs. The SEM images have the identical magnification.

collector during Li plating/stripping cycles at a current density of 0.1 mA cm^{-2} were observed using SEM (Figure 2). When using the bare Cu foil, Li deposits with irregular shapes and sizes were observed after Li plating at a capacity of 0.05 mAh cm^{-2} (Figure 2a). As the Li plating capacity was increased to 0.1 and 1.0 mAh cm^{-2}, the Li deposits grew larger and, eventually, a Li deposit layer having a porous and rough surface formed (Figures 2b and 3c). Further, after Li stripping at a capacity of 1.0 mAh cm^{-2}, substantial residues that could be SEI components and "dead Li" remained on the Cu foil (Figure 2d). In contrast, the changes in the Li morphology on Ni IO@Cu were completely different. When the Li plating capacity was 0.05 mAh cm^{-2}, Li deposits with relatively uniform shapes and sizes were formed on the Ni IO@Cu (Figure 2e). As the Li plating capacity was increased to 0.1 and 1.0 mAh cm^{-2}, the Li deposits grew larger and merged into wide and flat lumps, yielding a dense Li deposit layer with a smooth surface (Figure 2f and g). Further, when the Li was stripped at a capacity of 1.0 mAh cm^{-2}, the Li deposits almost completely disappeared from the surface of the Ni IO@Cu, and there was no sign of "dead Li", although a small amount of SEI material was observed (Figure 2h).

The Li plating/stripping behavior on Ni IO@Cu was highly stable and reversible in comparison to that on a bare Cu foil, as shown in Figure 2. To demonstrate the crucial role of 3D porous Ni IO framework in Li stabilization, the Li deposition behavior was investigated further (Figure S3). During the initial stages of Li deposition at a capacity of 0.02 mAh cm^{-2}, the Li deposits covered the whole surface of the Ni IO structure (Figure S3a and a'). On further plating to 0.05 mAh cm^{-2}, the Li deposits wrapping the surface of the Ni IO structure thickened, and distorted hemispherical Li deposits of approximately 3 μm in size were formed on the top surface of the Ni IO structure (Figure S3b and b'). As the Li plating capacity increased to 1.0 mAh cm^{-2}, the Li deposits continued to grow via lateral coalescence into wide, flat, and dense Li deposit layer (Figure S3c–f). These observations can be explained by the well-ordered pores of the 3D Ni IO structure and large surface area, which decreases the local current density and prevents charge concentration, resulting in stable Li deposition during the early stages of deposition.[31–34] Further, the flat and dense morphology is beneficial for subsequent Li deposition. Notably, the FIB-cut cross sectional SEM image after Li plating at a capacity of 0.1 mAh cm^{-2} revealed Li deposits occupying the undermost pores of the Ni IO structure (Figure S3c'), indicating that the Li deposits grew from the bottom of the Ni IO structure and filled the interconnected pores; this could contribute to the suppression of Li dendrite growth. On the basis of the SEM results, the initial nucleation and deposition of Li play a dominant role in the subsequent Li deposition behavior. Figure 2 (i and j) shows schematics of the Li growth behavior on bare Cu and Ni IO@Cu, respectively. The initial uneven Li
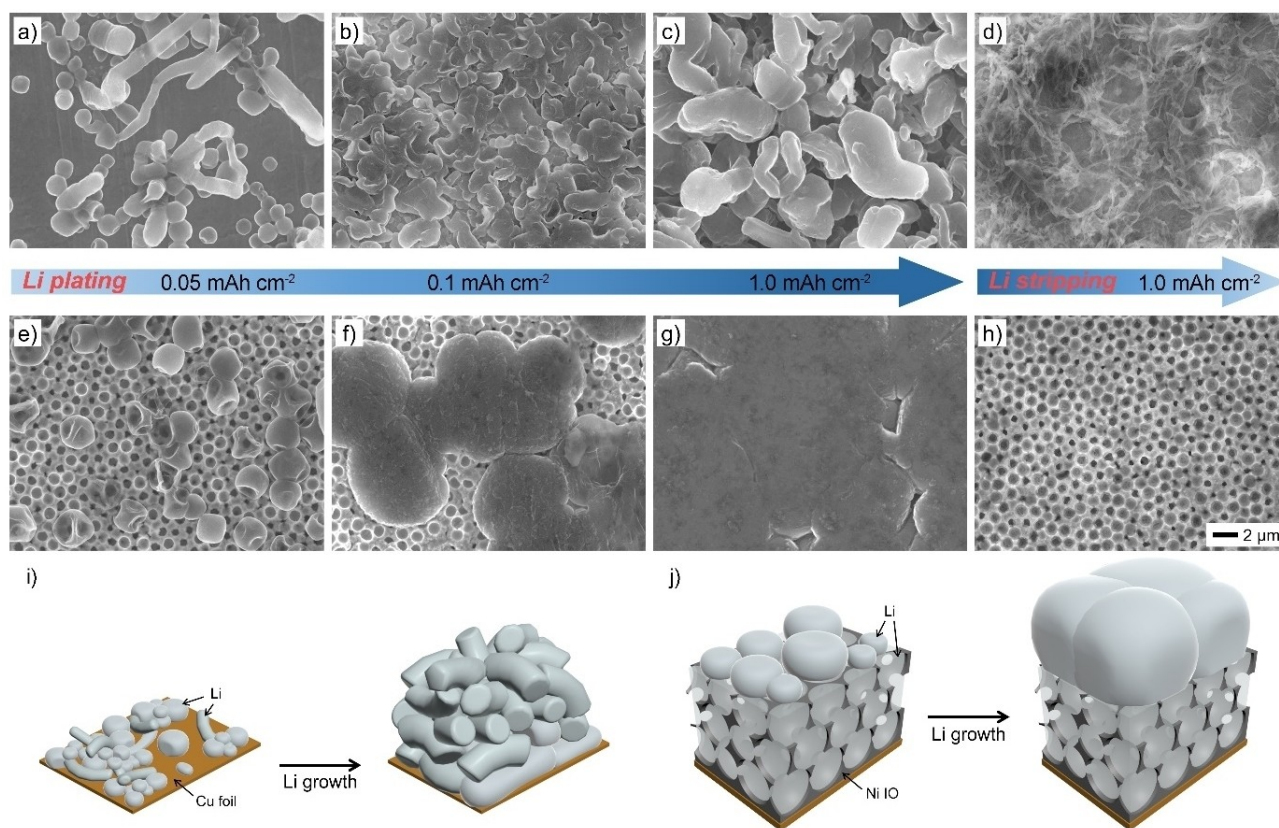
Figure 2. Morphological changes of Li deposits during Li plating and stripping on a–d) bare Cu and e–h) Ni IO@Cu at a current density of 0.1 mA cm^{-2} at varying capacities: Li plating at a capacity of a, e) 0.05, b, f) 0.1 and c, g) 1.0 mAh cm^{-2}, and d, h) stripping at a capacity of 1.0 mAh cm^{-2}. The SEM images have the identical magnification. Schematic illustrations for Li growth on i) bare Cu and j) Ni IO@Cu.

deposition on the bare Cu induced the formation of a rough and porous Li deposit layer (Figure 2i). In contrast, the initial stabilized Li deposition by the 3D Ni IO structure resulted in a flat and dense overlaying Li deposit layer (Figure 2j).

Encouraged by these results, the electrochemical performance of the prepared samples was evaluated in asymmetric cells by pairing Li foil with either bare Cu foil or Ni IO@Cu. Figure 3(a) shows plots of the CE of Li plating/stripping vs. cycle number of the cells with a cycling capacity of 1.0 mAh cm^{-2} at a current density of 1.0 mA cm^{-2}. In comparison to the bare Cu electrode, the Ni IO@Cu electrode demonstrated significantly improved cycle life (Figure 3a). Further, the CE of the cell using the Ni IO@Cu current collector was stable at more than 99% for approximately 120 cycles. In sharp contrast, CE of the cell using bare Cu rapidly decayed below 80% after the 10th cycle. Additionally, Figure S4 shows plots of the CE of Li plating/stripping vs. cycle number at a high current density of 2.0 mAh cm^{-2}, revealing the improved cycle life of the cell containing the Ni IO@Cu current collector compared to that using bare Cu.

In addition, the nucleation overpotential of Li on Ni IO@Cu was determined: 14 mV, which is far lower than that on bare Cu (38 mV, Figure 3b). Figure 3(c) shows the voltage profiles of the cells during the 10th Li plating/stripping cycle, clearly showing the much lower overpotential during cycling of Ni IO@Cu

compared to that of bare Cu. The lower overpotentials for the cell containing Ni IO@Cu can be explained as follows: i) the superior lithiophilicity of Ni than Cu,[50] ii) reduced local current density on Ni IO@Cu as a result of the enlarged surface area,[33,34] and iii) stable SEI formation on Ni IO@Cu.[32,33] As shown in Figure 2(d), a large amount of the SEI remained on the bare Cu foil after Li stripping, and this accumulated on repeated cycling, thus increasing the cell resistance. Next, EIS measurements after 10th Li plating/stripping cycle were carried out, and the cell using bare Cu showed relatively large electrolyte resistance and interfacial resistance compared to those of Ni IO@Cu, possibly because of the continuous electrolyte decomposition and accumulation of SEI components, respectively. This result is also consistent with the polarization behavior of the cells. Further, the SEM images of both electrodes after the 10th Li plating and stripping cycle further confirmed our speculation. A thin SEI layer covered the Ni IO surface, whereas a large amount of residue, including SEI components and "dead Li," remained on the bare Cu surface (Figure S5).

To evaluate the applicability of the Ni IO@Cu electrode as a current collector in Li metal batteries, the electrochemical performance of lithiated Ni IO@Cu was also investigated. First, the morphology of the Li deposit layers on bare Cu foil and Ni IO@Cu was examined using SEM. Even at an elevated current
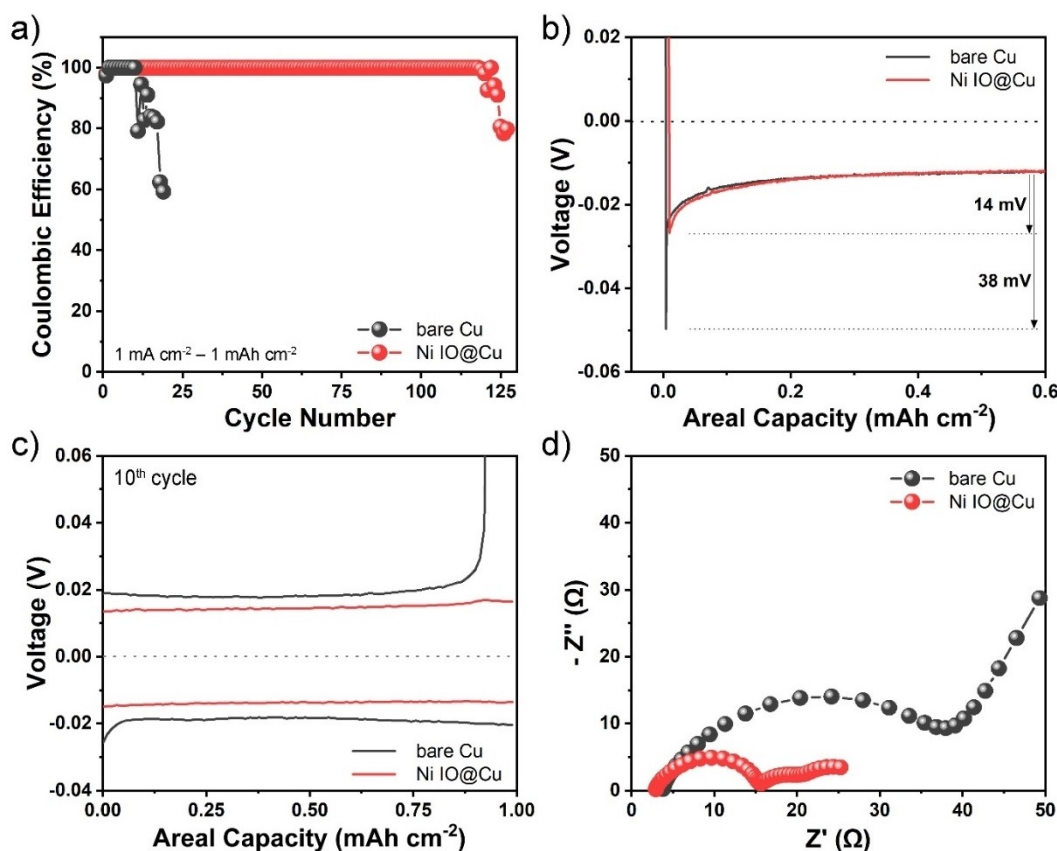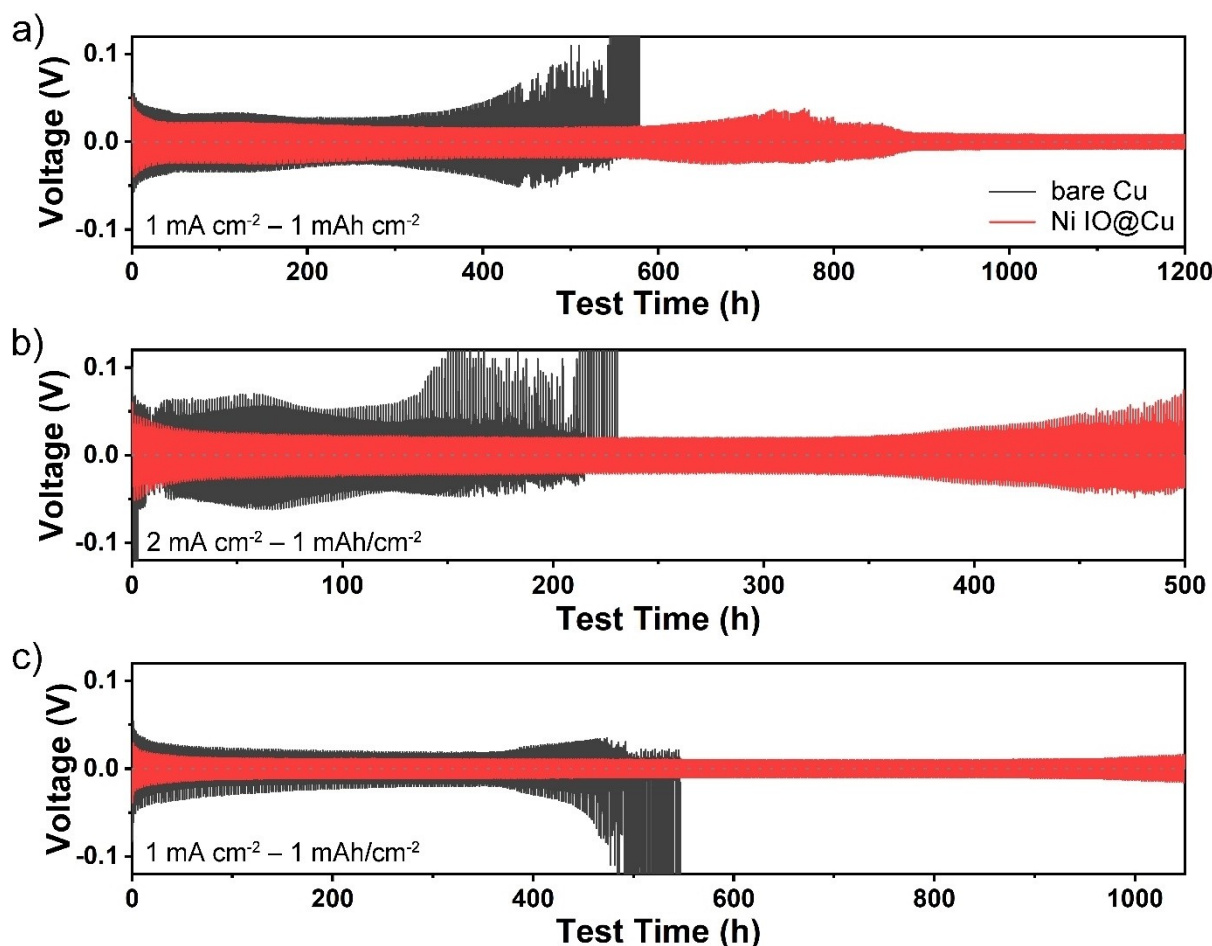

Figure 3. a) Coulombic efficiency of Li plating/stripping in asymmetric cells using bare Cu or the Ni IO@Cu, and Li foil at a capacity of 1 mAh cm^{-2} at a current density of 1 mA cm^{-2}. Li plating-stripping voltage profiles of the asymmetric cells during b) the initial Li plating, and c) 10th Li plating-stripping cycle. d) Nyquist plots of the asymmetric cells after 10th Li plating-stripping cycle.

density and capacity of $0.5\,mA\,cm^{-2}$ and $10.0\,mAh\,cm^{-2}$, respectively, the Li deposit layer on the Ni IO@Cu remained flat and dense, whereas that on bare Cu was rough and porous with Li dendrites (Figure S6b and e). The thickness of the Li deposit layers on bare Cu and the Ni IO@Cu after Li plating with the capacity of $10\,mAh\,cm^{-2}$ were approximately 113 and 73 µm, respectively, further confirming densely deposited Li on the Ni IO@Cu (Figure S6c and f).

Figures 4a and S7 show the voltage profiles for Li plating/stripping in asymmetric cells pairing Li foil with bare Cu or Ni IO@Cu. Li was plated on the samples first at a current density of $0.5\,mA\,cm^{-2}$ at a capacity of $10\,mAh\,cm^{-2}$ and then, Li stripping/plating was carried out at a current density of $1.0\,mA\,cm^{-2}$ and a capacity of $1.0\,mAh\,cm^{-2}$. The cell with the Ni IO@Cu current collector showed a more stable voltage response with relatively small fluctuations in the voltage hysteresis compared to those of the cell containing bare Cu. In addition, the cell with the Ni IO@Cu current collector showed much improved cycling stability compared to that containing bare Cu, for which the large voltage hysteresis of the cell shortened the cycle life. The EIS measurements conducted on the cells after lithiation and repetitive Li stripping/plating cycles revealed that the cell with the Ni IO@Cu current collector had smaller resistance compared to the cell with bare Cu, which is favorable for achieving a narrow voltage hysteresis and improving the cycle life of the cell (Figure S8). At a higher current density of $2.0\,mA\,cm^{-2}$, stable cycling with smaller voltage hysteresis was also achieved in the Ni IO@Cu cell, whereas that containing bare Cu showed a dramatic increase in the voltage hysteresis and a shorter cycle life (Figures 4b and S9). Li plating/stripping tests at even higher current densities or with higher cycling capacity also showed the superior electrochemical performance of the cell containing Ni IO@Cu in comparison to that containing bare Cu (Figures S10 and S11). In addition, the Li plating/stripping was studied using symmetric cells with either lithiated bare Cu or Ni IO@Cu. In the same manner, the cell containing Ni IO@Cu exhibited much improved electrochemical performance: a more stable voltage response and far longer cycle life than that containing bare Cu (Figures 4c and S12). The remarkably improved electrochemical performance of the Ni IO@Cu cell can be attributed to the stable nucleation and growth of Li on the Ni IO@Cu current


Figure 4. Voltage profiles of Li plating/stripping in asymmetric cells using pre-lithiated bare Cu or the Ni IO@Cu, and Li foil at different cycling capacities at different current densities: a) $1\,mA\,cm^{-2}-1\,mAh\,cm^{-2}$ and b) $2\,mA\,cm^{-2}-1\,mAh\,cm^{-2}$. c) Voltage profiles of Li plating/stripping in symmetric cells using pre-lithiated bare Cu or the Ni IO@Cu with a cycling capacity of $1\,mAh\,cm^{-2}$ at a current density of $1\,mA\,cm^{-2}$. The pre-lithiation was done with a capacity of $10\,mAh\,cm^{-2}$ at a current density of $0.5\,mA\,cm^{-2}$.

collector arising from the 3D porous structure with a large surface area.

On the basis of the electrochemical results and SEM observations, the Ni IO@Cu structure encouraged the stable growth of Li, resulting in enhanced electrochemical performance. To emphasize the importance of the enhanced stability as a result of using the Ni IO@Cu structure, galvanostatic charge/discharge cycling was performed for both LIB and Li–S battery cells with pre-lithiated Ni IO@Cu and bare Cu as anodes. LIB full cells containing LiFePO₄ cathodes were cycled at 2 and 4 C after formation cycles at 0.1 C. One of the strong points of LMBs is their high energy densities, so a relatively small amount of Li was used in the full cells. Previously, relatively large excesses of Li with respect to the cathode capacity have been used for LIB full cell characterization.[32,34,36,41,43] In this study, the small amount of Li was pre-lithiated on the Ni IO@Cu or bare Cu as anodes to yield the LIB full cells (Table S1). During the initial galvanostatic cycle at 0.1 C, the cells containing either pre-lithiated bare Cu or Ni IO@Cu displayed nearly identical voltage profiles with a specific capacity of 154 mAh g⁻¹ (Figure 5a). In comparison to the cells containing pre-lithiated bare Cu cells, those containing pre-lithiated, Ni IO@Cu exhibited remarkably improved cycling stabilities at both 2 and 4 C (Figure 5b). Specifically, on cycling at 2 C, the cells delivered almost the same specific capacities (125 and 126 mAh g⁻¹ for Ni IO@Cu and bare Cu, respectively) in the first cycle. However, after 100 cycles, the cells containing Ni IO@Cu still

retained 89.4% of the initial capacity, whereas the cell containing bare Cu retained only 63.7% of the initial capacity. Further, when the current density was increased to 4 C, the cell containing Ni IO@Cu delivered a capacity of 107.6 mAh g⁻¹ during the 1st cycle and retained 70.2% of its initial capacity after 100 cycles. In contrast, the specific capacity of the cell with bare Cu significantly reduced from 98.6 mAh g⁻¹ during the 1st cycle and maintained only 31.6% of its initial capacity after 100 cycles.

Lithiated Ni IO@Cu and bare Cu were also tested in a Li–S battery as anodes. The cells showed typical voltage profiles of Li–S cells, yielding specific capacities of 865.6 and 848.0 mAh g⁻¹ at 0.1 C for Ni IO@Cu and bare Cu, respectively (Figure 5c). Although both cells showed considerable capacity fading over approximately 100 cycles, possibly because of the dissolution of Li polysulfides in the electrolyte,[51] the cell containing the Ni IO@Cu current collector retained 56% of its initial capacity (365.3 mAh g⁻¹) after 400 cycles (Figure 5d). In contrast, the specific capacity of the cell with bare Cu gradually decayed and maintained only 44.7% of its initial capacity after 400 cycles. The much improved cycle stability of the cells containing Ni IO@Cu compared to those having bare Cu can be attributed to the uniform Li deposition and dissolution on the Ni IO@Cu, which resulted from the lowered local current density as a result of the large surface area of the structure and interconnected pores.
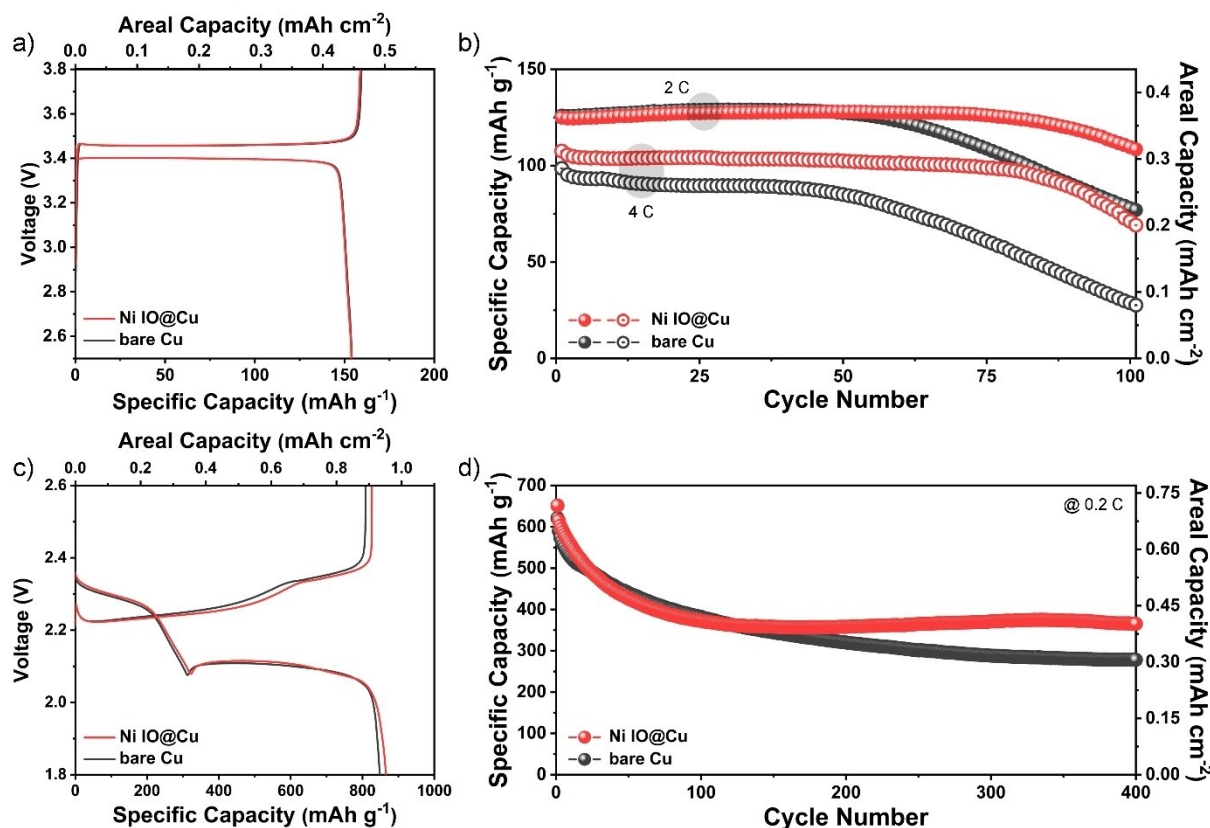
Figure 5. a) Galvanostatic charge/discharge voltage profiles of pre-lithiated bare Cu or the Ni IO@Cu//LFP LIB full cells at 0.1 C. b) Cycle stability of the LIB full cells at 2 and 4 C. c) Galvanostatic charge/discharge voltage profiles of Li–S cells using pre-lithiated bare Cu or the Ni IO@Cu at 0.1 C. d) Cycle stability of the Li–S cells at 0.2 C.

3. Conclusions

In summary, we successfully fabricated a Ni IO@Cu current collector via the self-assembly of PS particles and electrodeposition of Ni, which filled the pores in the PS colloidal crystal. Thanks to its structural advantages, such as interconnected pores and large surface area, the Ni IO@Cu acted as an excellent current collector for Li. We found that stable SEI formation and the deposition of a smooth, dense, and conformal Li layer in the early stages of plating were extremely important because these determine the morphology of the subsequent Li deposits. In particular, the use of bare Cu induced the formation of a rough and porous Li deposit layer, whereas Li growth on the Ni IO@Cu current collector was stable, yielding a flat and dense Li deposit, which contributed to the reduced local current density, suppressed Li dendrite growth and "dead Li" formation. In addition, SEI formation was stable on the Ni IO@Cu surface. Crucially, the formation of a smooth, dense Li deposit layer on Ni IO@Cu resulted in improved Li plating/stripping performance in terms of a narrower voltage hysteresis and longer cycle life compared to those of cells containing bare Cu. Furthermore, LIB and Li–S battery cells with the Ni IO@Cu current collector also exhibited substantially enhanced cycle stability compared to those with bare Cu current collectors. The results of this study indicate the significance of Li morphology control for improving the electrochemical performance of LMBs. However, further studies on structural optimization, increasing the lithophilicity of the structure, and systematic investigation of electrolyte effects are needed to bring LMBs closer to commercialization.

Experimental Section

Materials

A styrene monomer (Sigma-Aldrich), ammonium persulfate (APS, Sigma-Aldrich), poly(vinylpyrrolidone) (PVP, Sigma-Aldrich, $M_w =$ 10,000 and 55,000), nickel sulfate (Sigma-Aldrich), nickel chloride (Junsei), boric acid (Sigma-Aldrich), and sodium dodecyl sulfate (SDS, Junsei) were purchased and used as received. In all experiments, we used deionized (DI) water with a resistivity of 18.2 MΩ, which was prepared using a Milli-Q ultrapure water system (Millipore).

Preparation of PS opal structure on a Cu foil

PS particles were synthesized using dispersion polymerization.[48] PVP (0.03 g, $M_w =$ 10,000) and styrene monomer (6.6 mL) was added to isopropyl alcohol (75 mL) in a vial and kept at 70 °C upon stirring. Then, APS aqueous solution (9 mL, 20 mmol) was added into the vial as an initiator and kept at 70 °C with sufficient stirring for 18 h. After polymerization, colloidal suspension was centrifuged, washed off repeatedly with ethanol, and finally dispersed in DI water. Next, PS opal structure on a Cu foil was fabricated by a colloidal self-assembly technique. A Cu foil was cleaned with sulfuric acid in aqueous solution (0.1 mol) and acetone, respectively, before use. To assemble 3D colloidal crystals, Cu foils were dipped vertically into a PS colloidal suspension (0.1 wt%, 40 mL) containing PVP ($M_w =$ 55,000) aqueous solution (0.5 wt%, 0.1 mL). Then, colloidal suspensions were dried in an oven at 65 °C until

completely dry. To enhance the connection strength between colloidal PS particles, and PS colloidal crystal and the Cu foil, the samples were annealed at 95 °C for 5 h.

Preparation of the 3D porous Ni IO@Cu: Ni electrodeposition solution was prepared by dissolving nickel sulfate (50 g), nickel chloride (12 g), boric acid (8 g), and SDS (1 g) in DI water (200 mL). The Cu foil with PS colloidal template was assembled into a homemade cell made by Teflon™. With a pure Ni plate as a counter electrode, Ni was electrodeposited into 3D PS colloidal template on Cu foil at a current density of 0.4 mA cm^{-2} for 15,000 s. After completion of the electrodeposition, the sample was rinsed with DI water and the PS colloidal template was then dissolved with tetrahydrofuran (THF).

Characterizations

The morphology of fabricated samples and morphological evolution of Li were studied using a field-emission scanning electron microscope (FE-SEM, JSM-6700F, JEOL) at an accelerating voltage of 10 kV. Cross-sectional view SEM images of Li deposits were taken using a focused ion beam-SEM (FIB-SEM, Crossbeam 550, ZEISS). X-ray diffraction (XRD) pattern was obtained with an X-ray diffractometer (Ultima IV, Rigaku) using Cu K_α ($\lambda = 1.5418$ Å) radiation at a power of 45 kV.

Electrochemical measurements

To evaluate the electrochemical performance of the samples, CR2032 coin-type cells with both asymmetric and symmetric configurations were assembled in an Ar-filled glove box (H$_2$O < 1 ppm, MBraun). Asymmetric cells were assembled using either bare Cu foil or Ni IO@Cu as working electrodes and Li foil with a thickness of 300 μm (Honjo Metal Co., Ltd.) as a counter and reference electrodes. Meanwhile, electrodes for symmetric cells were prepared by Li plating on either bare Cu foil or Ni IO@Cu at a capacity of 10 mAh cm^{-2} at a current density of 0.5 mA cm^{-2} in asymmetric cells. The cells were then disassembled and re-assembled using either two lithiated bare Cu foils or lithiated Ni IO@Cu. As a separator and an electrolyte, polyethylene separator (Hipore SV718, Asahi Kasei) and bis(trifluoromethylsulfonyl)imide (LiTFSI, Sigma-Aldrich, 1 mol) in 1,2-dimethoxymethane (DME, Sigma-Aldrich)/1,3-dioxolane (DOL, Sigma-Aldrich) (1:1 v/v) with LiNO$_3$ (0.2 mol, Sigma-Aldrich) were used. To exclude volume influence of an electrolyte, the same amount of electrolyte (75 μL) was used in all experiments. The charge and discharge tests were carried out using a battery tester (WBCS3000 L, WonATech). Electrochemical impedance spectroscopy (EIS) was tested with a frequency range between 1.0 MHz to 50 mHz using a potentiostat (VMP3, Biologic).

For evaluating the electrochemical performance of battery cells containing bare Cu foil or Ni IO@Cu, CR2032 coin-type Li-ion and Li–S cells were assembled. LiFePO$_4$ (LFP) cathode with a loading density of 2.9 mg cm^{-2} was fabricated by casting a slurry containing LFP powder, Super P carbon black, and polyvinylidene fluoride (PVDF) binder at a mass ratio of 8:1:1 in NMP onto an Al foil current collector. Cathode for Li–S cell with a loading density of 1.1 mg$_s$ cm^{-2} was fabricated by casting a slurry containing S powder (Sigma-Aldrich), Super P, and PVDF binder at a mass ratio of 7:2:1 in NMP onto an Al foil current collector. Lithiated bare Cu or Ni IO@Cu at a capacity of 0.25 mAh cm^{-2} for LIB and 10 mAh cm^{-2} for Li–S battery were used as anodes. LFP full cells were galvanostatically cycled between 2.5 and 3.8 V vs. Li/Li$^+$ at 2.0 or 4.0 C after two formation cycles at 0.1 C. Li–S full cells were galvanostatically cycled between 1.8 and 2.6 V vs. Li/Li$^+$ at 0.2 C after a formation cycle at 0.1 C.

Supporting Information

Supporting Information is available from the Wiley Online Library or from the author.

Acknowledgements

Conflict of Interest

The authors declare no conflict of interest.

[1] D. Larcher, J.-M. Tarascon, *Nat. Chem.* **2015**, *7*. 19–29.
[2] Y. Ding, Z. P. Cano, A. Yu, J. Lu, Z. Chen, *Electrochem. Energy Rev.* **2019**, *2*, 1–28.
[3] Y. Miao, P. Hynan, A. von Jouanne, A. Yokochi, *Energies* **2019**, *12*, 1074.
[4] X. Yuan, F. Ma, L. Zuo, J. Wang, N. Yu, Y. Chen, Y. Zhu, Q. Huang, R. Holze, Y. Wu, T. van Ree, *Electrochem. Energy Rev.* **2021**, *4*, 1–34.
[5] J. Li, Z. Du, R. E. Ruther, S. J. An, L. A. David, K. Hays, M. Wood, N. D. Phillip, Y. Sheng, C. Mao, S. Kalnaus, C. Daniel, D. L. Wood III, *JOM* **2017**, *69*, 1484–1496.
[6] J. U. Choi, N. Voronina, Y.-K. Sun, S.-T. Myung, *Adv. Energy Mater.* **2020**, *10*, 2002027.
[7] A. Chakraborty, S. Kunnikuruvan, S Kumar, B Markovsky, M Dixit, D. T. Major, *Chem. Mater.* **2020**, *32*, 915–952.
[8] S.-T. Myung, F. Maglia, K.-J. Park, C. S. Yoon, P. Lamp, S.-J. Kim, Y.-K. Sun, *ACS Energy Lett.* **2017**, *2*, 196–223.
[9] J. Asenbauer, T. Eisenmann, M. Kuenzel, A. Kazzazi, Z. Chen, D. Bresser, *Sustain. Energy Fuels* **2020**, *4*, 5387–5416.
[10] Y. Liu, D. Gao, H. Xiang, X. Feng, Y. Yu, *Energy Fuels* **2021**, *35*, 12921–12937.
[11] W. Xu, J. Wang, F. Ding, X. Chen, E. Nasybulin, Y. Zhang, J.-G. Zhang, *Energy Environ. Sci.* **2014**, *7*, 513–537.
[12] J.-G. Zhang, W. Xy, J. Xiao, X. Cao, J. Liu, *Chem. Rev.* **2020**, *120*, 13312–13348.
[13] H. Wu, D. Zhuo, D. Kong, Y. Cui, *Nat. Commun.* **2014**, *5*, 5193.
[14] X.-R. Chen, C. Yan, J.-F. Ding, H.-J. Peng, Q. Zhang, *J. Energy Chem.* **2021**, *62*, 289–294.
[15] S.-K. Jeong, H.-Y. Seo, D.-H. Kim, H.-K. Han, J.-G. Kim, Y. B. Lee, Y. Iriyama, T. Abe, Z. Ogumi, *Electrochem. Commun.* **2008**, *10*, 635–638.
[16] J. Zian, W. A. Henderson, W. Xu, P. Bhattacharya, M. Engelhard, O. Borodin, J.-G. Zhang, *Nat. Commun.* **2015**, *6*, 6362.
[17] L. Suo, W. Xue, M. Gobet, S. G. Greenbaum, C. Wang, Y. Chen, W. Yang, Y. Li, J. Li, *Proc. Natl. Acad. Sci. USA* **2018**, *115*, 1156–1161.
[18] F. Ding, W. Xu, G. L. Graff, J. Zhang, M. L. Sushko, X. Chen, Y. Shao, M. H. Engelhard, Z. Nie, J. Xiao, X. Liu, P. V. Sushko, J. Liu, J.-G. Zhang, *J. Am. Chem. Soc.* **2013**, *135*, 4450–4456.
[19] C. Ma, Y. Feng, F. Xing, L. Zhou, Y. Yang, Q. Xia, L. Zhou, L. Zhang, L. Chen, D. G. Ivey, D. R. Sadoway, W. Wei, *J. Mater. Chem. A* **2019**, *7*, 19970–19976.
[20] Y. Lu, S. K. Das, S. S. Moganty, L. A. Archer, *Adv. Mater.* **2012**, *24*, 4430–4435.
[21] C. Yang, L. Zhang, B. Liu, S. Xu, T. Hamann, D. McOwen, J. Dai, W. Luo, Y. Gong, E. D. Wachsman, L. Hu, *Proc. Natl. Acad. Sci. USA* **2018**, *115*, 3770–3775.
[22] T. Jiang, P. He, G. Wang, Y. Shen, C.-W. Nan, L.-Z. Fan, *Adv. Energy Mater.* **2020**, *10*, 1903376.
[23] Z. Wang, X. Li, Y. Chen, K. Pei, Y.-W. Mai, S. Zhang, J. Li, *Chem* **2020**, *6*, 2878–2892.
[24] N. W. Li, Y. X. Yin, C. P. Yang, Y. G. Guo, *Adv. Mater.* **2016**, *28*, 1853–1858.
[25] N. W. Li, Y. Shi, Y. X. Yin, X. X. Zeng, J. Y. Li, C. J. Li, L. J. Wan, R. Wen, Y. G. Guo, *Angew. Chem. Int. Ed.* **2018**, *57*, 1505–1509; *Angew. Chem.* **2018**, *130*, 1521–1525.
[26] A. C. Kozen, C. F. Lin, O. Zhao, S. B. Lee, G. W. Rubloff, M. Noked, *Chem. Mater.* **2017**, *29*, 6298–6307.
[27] Z. Hu, S. Zhang, S. Dong, W. Li, H. Li, G. Cui, L. Chen, *Chem. Mater.* **2017**, *29*, 4682–4689.
[28] M. Liu, N. Deng, J. Ju, L. Wang, G. Wang, Y. Ma, W. Kang, J. Yan, *ACS Appl. Mater. Interfaces* **2019**, *11*, 17843–17852.
[29] Y. Liu, Q. Liu, L. Xin, Y. Liu, F. Yang, E. A. Stach, J. Xie, *Nat. Energy* **2017**, *2*, 1–10.
[30] Y. Li, W. Wang, X. Liu, E. Mao, M. Wang, G. Li, L. Fu, Z. Li, A. Y. S. Eng, Z. W. She, Y. Sun, *Energy Storage Mater.* **2019**, *23*, 261–268.
[31] G. Hou, X. Ren, X. Ma, L. Zhang, W. Zhai, Q. Ai, X. Xu, L. Zhang, P. Si, J. Feng, F. Ding, L. Ci, *J. Power Sources* **2018**, *386*, 77–84.
[32] L. M. Wang, Z. F. Tang, J. Lin, X. D. He, C. S. Chen, C. H. Chen, *J. Mater. Chem. A* **2019**, *7*, 17376–17385.
[33] H. Zhao, D. Lei, Y. He, Y. Yuan, Q. Yun, B. Ni, W. Lv, B. Li, Q. H. Yang, F. Kang, J. Lu, *Adv. Energy Mater.* **2018**, *8*, 1800266.
[34] S.-H. Wang, Y.-X. Yin, T.-T. Zuo, W. Dong, J.-Y. Li, J.-L. Shi, C.-H. Zhang, N.-W. Li, C.-Ju Li, Y.-G. Guo, *Adv. Mater.* **2017**, *29*, 1703729.
[35] B. Horstmann, J. Shi, R. Amine, M. Werres, X. He, H. Jia, F. Hausen, I. Cekic-Laskovic, S. Wiemers-Meyer, J Lopez, D. Galvez-Aranda, F. Baakes, D. Bresser, C.-C. Su, Y. Xu, W. Xu, P. Jakes, R.-A. Eichel, E. Figgemeier, U. Krewer, J. M. Seminario, P. B. Balbuena, C. Wang, S. Passerini, Y. S. Horn, M. Winter, K. Amine, R. Kostecki, A. Latz, *Energy Environ. Sci.* **2021**, *14*, 5289–5314.
[36] X. Ke, Y. Liang, L. Ou, H. Liu, Y. Chen, W. Wu, Y. Cheng, Z. Guo, Y. Lai, P. Liu, Z. Shi, *Energy Storage Mater.* **2019**, *23*, 547–555.
[37] S.-S. Chi, Y. Liu, W.-L. Song, L.-Z. Fan, Q. Zhang, *Adv. Funct. Mater.* **2017**, *27*, 1700348.
[38] J. Wang, M. Wang, F. Chen, Y. Li, L. Zhang, Y. Zhao, C. Chen, *Energy Storage Mater.* **2021**, *34*, 22–27.
[39] Q. Li, S. Zhu, Y. Lu, *Adv. Funct. Mater.* **2017**, *27*, 1606422.
[40] C. Chen, S. Li, P. H. L. Notten, Y. Zhang, Q. Hao, X. Zhang, W. Lei, *ACS Appl. Mater. Interfaces* **2021**, *13*, 24785–24794.
[41] Y. Shi, Z. Wang, H. Gao, J. Niu, W. Ma, J. Qin, Z. Peng, Z. Zhang, *J. Mater. Chem. A* **2019**, *7*, 1092–1098.
[42] X. Fei, Z. Dong, B. Gong, X. Zhao, *ACS Appl. Mater. Interfaces* **2021**, *13*, 42266–42275.
[43] T. T. Zuo, X.-W. Wu, C.-P. Yang, Y.-X. Yin, H. Ye, N.-W. Li, Y.-G. Guo, *Adv. Mater.* **2017**, *29*, 1700389.
[44] W. Deng, W. Zhu, X. Zhou, Z. Liu, *Energy Storage Mater.* **2018**, *15*, 266–273.
[45] Y. Zhang, W. Luo, C. Wang, Y. Li, C. Chen, J. Song, J. Dai, E. M. Hitz, S. Xu, C. Yang, Y. Wang, L. Hu, *Proc. Natl. Acad. Sci. USA* **2017**, *114*, 3584–3589.
[46] H. Kwon, J.-H. Lee, Y. Roh, J. Baek, D. J. Shin, J. K. Yoon, H. J. Ha, J. Y. Kim, H.-T. Kim, *Nat. Commun.* **2021**, *12*, 5537.
[47] R. Pathak, K. Chen, F. Wu, A. U. Mane, R. V. Bugga, J. W. Elam, Q. Qiao, Y. Zhou, *Energy Storage Mater.* **2021**, *41*, 448–465.
[48] S. T. Ha, O. Park, S. H. Im, *Macromol. Res.* **2010**, *18*, 935–943.
[49] D. Y. Kim, J. Suk, D. W. Kim, Y. Kang, S. H. Im, Y. Yang, O. Park, *J. Mater. Chem. A* **2014**, *2*, 6396–6401.
[50] K. Yan, Z. Lu, H. W. Lee, F. Xiong, P. C. Hsu, Y. Li, J. Zhao, S. Chu, Y. Cui, *Nat. Energy* **2016**, *1*, 1–8.
[51] E. S. Shin, K. Kim, S. H. Oh, W. I. Cho, *Chem. Commun.* **2013**, *49*, 2004–2006.